



Monitoring the Fault Zone of the Sefid Sang Earthquake (April 5, 2017, Mw 6.1) via Ambient Seismic Noise Analysis Utilizing the Moving Window Cross-Spectral Technique

Nameni, M. R.¹  | Rahimi, H.¹  | Mortezaejad, Gh.² 

1. Department of Seismology, Institute of Geophysics, University of Tehran, Tehran, Iran.

2. School of Earth Sciences, Damghan University, Damghan, Iran.

Corresponding Author E-mail: rahimih@ut.ac.ir

(Received: 20 Sep 2023, Revised: 10 Aug 2024, Accepted: 4 Jan 2025, Published online: 15 March 2025)

Abstract

The Passive Image Interferometry (PII) approach, which incorporates a cross-correlation process to reconstruct the green function between two stations, is emerging as an effective tool for studying seismic velocity changes. These changes provide significant information about the earth's structural and mechanical properties between the stations. Despite its numerous benefits, monitoring fault zones with PII can be challenging due to various processes that can cause velocity changes in the crust. In this study, we investigated the usefulness of this method on the noise recorded in two seismic stations near the fault zone that caused the Sefid-Sang earthquake with a magnitude of $M_w = 6.1$. Our study covers a period of 15 months, including 12 months before and three months after the earthquake. We investigated velocity changes across different frequency ranges and examined the effect of stacking on the results. Our analysis revealed a 0.3% increase in seismic velocity two months before the earthquake.

Keywords: Interferometry, Passive image, Cross-correlation, green function, Iran.

1. Introduction

Understanding the temporal variations in the Earth's structure is crucial for various geophysical applications, particularly in the context of hydrocarbon reservoirs, volcanic activity, and fault zones. These variations can significantly affect the elastic response of the Earth's crust, making seismic response analysis an effective method for studying these changes (Crampin & Zatsepin, 1997). Seismic coda waves and ambient noise are particularly valuable for this purpose due to their random and repeated sampling, which enhances sensitivity to minor alterations in the elastic properties of the Earth (Grêt, 2006).

The passive imaging technique, pioneered by Campillo and Paul (2003) has demonstrated the potential to retrieve the Green's function between seismological stations using coda waves generated by earthquakes. This method has been instrumental in understanding the dynamic response of the Earth's crust, especially in tectonically active and volcanic regions where stress changes may precede seismic events. Previous studies have shown that variations in coda wave amplitude can

indicate potential volcanic activity (Gret et al., 2005), while the coda wave interferometry method has confirmed observable crustal changes before earthquakes (Wegler, 2007). Recently, there has been a growing interest in utilizing ambient seismic noise to recover the Green's function between seismometers through cross-correlation techniques. This approach enables continuous monitoring of seismic velocity changes, providing insights into the temporal evolution of the Earth's subsurface (Sens-Schoenfelder and Wegler, 2006; Sens-Schönfelder & Wegler, 2007). The primary objective of this study is to investigate the effectiveness of the moving window cross-spectral technique in analyzing ambient seismic noise recorded at two stations near the fault zone of the Sefid-Sang earthquake ($M_w 6.1$), which occurred in Iran. This paper is organized as follows: Section 2 discusses the geological and seismic context of the 2017 Sefid Sang earthquake, including its tectonic setting, fault mechanism, and seismic hazards. Section 3 outlines the methodology employed in this study, detailing

Cite this article: Nameni, M. R., Rahimi, H., & Mortezaejad, Gh. (2025). Monitoring the Fault Zone of the Sefid Sang Earthquake (April 5, 2017, Mw 6.1) via Ambient Seismic Noise Analysis Utilizing the Moving Window Cross-Spectral Technique. *Journal of the Earth and Space Physics*, 50(4), 15-26. DOI: <http://doi.org/10.22059/jesphys.2025.363221.1007545>

E-mail: (1) nameni.mreza@ut.ac.ir (2) g.mortezaejad@du.ac.ir



the data collection and analysis techniques used to monitor changes in seismic velocity. Section 4 discusses the significance of these findings in relation to existing literature and suggests directions for future research.

2. Geological and Seismic Context

2-1. Tectonic Setting of the 2017 Sefid Sang Earthquake

The 2017 Mw 6.1 Sefid Sang earthquake struck northeastern Iran, a tectonically active region situated between the Kopetdag Mountains and the Binalud Range (Aflaki et al., 2019; Nedaei and Alizadeh, 2020; Ghayournajarkar and Fukushima, 2020). This area is characterized by complex geological structures, significant elevation changes, and a history of notable earthquakes, indicating ongoing seismic activity (Aflaki et al., 2019; Petrova et al., 2022). Northeastern Iran lies at the boundary between the Arabian and Eurasian plates, with the Kopetdag Mountains and the Binalud range serving as primary deformation belts. The region has a complex geological history involving continental collision, subduction, and rifting, contributing to its geological instability (Petrova et al., 2022).

2-2. Fault Mechanism and Coseismic Displacements

The Sefid Sang earthquake is associated with a blind reverse fault, with analyses using InSAR data providing insights into its fault mechanics and coseismic displacements (Aflaki et al., 2019; Nedaei and Alizadeh, 2020). The InSAR analysis revealed a northeast-dipping fault with a strike angle of approximately 314.8 and a dip angle of 47.4. The maximum observed displacements reached up to 14.2 cm (Nedaei and Alizadeh, 2020).

2-3. Seismic Hazard and Vulnerability

Despite the low population density, the Sefid Sang earthquake caused significant damage, affecting 40-100% of buildings in several villages and resulting in fatalities. The event highlights the vulnerability of northeastern Iran to significant seismic events and underscores the importance of monitoring and understanding the region's geological context (Aflaki et al., 2019; Petrova et al., 2022). The ongoing tectonic movements in the region, as suggested by the interferogram patterns,

emphasize the need for detailed monitoring of seismic activity (Nedaei and Alizadeh, 2020). The distribution of aftershocks following the earthquake also emphasizes the active tectonics of the area and the potential for future seismic events (Petrova et al., 2022).

3. Methodology

3-1. data collection

This study utilized continuous ambient noise data from the TBJM and JRKH stations of the Mashhad seismological network, affiliated with the Iranian Seismological Center of Tehran University Geophysics Institute. These stations are equipped with broadband seismometers capable of recording a wide range of seismic waves. The sensitivity of broadband sensors allows for the detection of low-magnitude earthquakes, making these stations effective for monitoring seismic activity. Broadband seismometers typically have a frequency response ranging from 0.01 Hz to 100 Hz, allowing them to capture both long-period and short-period seismic waves. The dynamic range of broadband sensors is generally high, enabling them to record both very weak and very strong seismic signals without distortion. These stations operate continuously, transmitting data in real-time to the Iranian Seismological Center for analysis and monitoring. Data were collected for a period of 15 months, including 12 months before and three months after the Sefid-Sang earthquake (Mw=6.1). The earthquake's epicenter was recorded at 35.85 degrees latitude and 60.34 degrees longitude with a depth of 10 km, located between the two observed stations, which were 71 km apart (Figure 1).

3-2. Pre- processing

Pre-processing involves several systematic steps to prepare waveform data for analysis. Initially, pairs of data are split, and a list of stations is created while querying the database to retrieve file paths for each station. For each station, all files containing data for a specific day are opened, and the traces are merged and segmented to form the most continuous segments possible. Each segment or chunk, is processed by removing the mean value to center the data around zero (demeaning), applying a tapering function to reduce edge effects (tapering), and combining the processed chunks into a single continuous

trace for the day (merging). If a chunk does not align with the sampling grid, it is phase-shifted in the frequency domain, requiring additional tapering and fitting. Small gaps between chunks can be filled with interpolated values, while larger gaps may be addressed by modifying the frequency content of the existing time series (Nameni et al., 2024). Each daily trace undergoes high-pass filtering at a specified frequency and, if necessary, low-pass filtering. The trace is then decimated or downsampled, with downsampling allowing for flexible reduction by any factor using the ObsPy Lanczos resampler. If configured, the daily trace is corrected for instrument response, supporting formats such as dataless seed and inventory XML. The preprocessing routine outputs a Stream object containing all processed traces for all stations and components. This systematic approach ensures that the waveform data is well-prepared for subsequent analysis, which may include further signal processing or interpretation in seismic studies.

3-3. Passive Imaging Technique

The passive imaging technique employed in this study involves the use of ambient seismic noise to monitor changes in seismic velocity. This method allows for the reconstruction of the Green's function between two seismic stations, providing insights into the dynamic response of the Earth's crust.

3-4. Moving Window Cross-Spectral Technique (MWCS)

The MWCS method was initially presented by Poupinet et al. (1984) as a tool for recovering relative velocity fluctuations between doublet earthquakes. More recently, Brenguier et al. (2008) applied this technique in seismic noise records, where noise cross-correlations were treated analogous to doublets.

The moving window cross-spectral technique is utilized to analyze time-series data obtained by correlating noise sequences collected from two separate seismic stations. This technique operates in the frequency domain, allowing for the definition of the bandwidth of coherent signals within the correlation function.

In our study, the sensitivity kernel is a key element in understanding seismic velocity variations over time. It is computed using the finite-frequency theory, which considers the wave propagation in the Earth's medium as a

volumetric process rather than a simple ray-based approximation. Specifically, the sensitivity kernel provides information on how seismic travel times respond to velocity changes in different regions, helping to pinpoint the exact locations where stress-related changes occur.

The kernel is calculated by integrating travel time perturbations over the volume of the Earth's structure between two seismic stations. This approach is enhanced by the adjoint method (Tape et al., 2010; Tromp et al., 2005), which allows for backward propagation of the seismic wavefield from the receiver to the source. By analyzing the phase shifts in the cross-spectral domain between the reference and current functions at different frequencies, the time delay (δt) and relative velocity perturbations ($\delta v/v$) are determined. The sensitivity kernel is then used to relate these measurements to specific layers of the Earth's subsurface.

However, the kernel calculation involves several assumptions and limitations, it assumes homogeneous velocity perturbations across the study volume, which may not account for localized changes in complex geological settings. Moreover, the resolution of velocity changes is frequency-dependent, with lower frequencies penetrating deeper into the Earth but providing less spatial resolution. This trade-off affects the interpretation of deeper layers.

3-5. Calculation of Time Delay

The initial phase of the process involves building at least one reference cross-correlation and several current cross-correlations. Since the noise records are long and need to be processed computationally, they are divided into shorter sequences (for example, one sequence for each day or hour). Several cross-correlations are then stacked to create the reference and current functions. These functions are defined by the number of stacked cross-correlations, where the reference function (N_{ref}) must be significantly larger than the current function (N_{cur}) to ensure that the reference, cc_{ref} , provides a background value, while the current, cc_{cur} , provides valuable information on the current state of the Earth's crust.

For any pair of functions (cc_{ref} and cc_{cur}) used as reference and current respectively, a two-step technique is employed.

Time Delay Determination: The first step involves determining the time delay between the two signals within a set of overlapping windows.

Relative Velocity Variation Calculation: The second step consists of calculating the variation in relative velocity associated with the current function in comparison to the reference.

In the second step, for the sake of simplicity, it is assumed that there is a homogeneous perturbation in the seismic wave propagation velocity within the studied medium.

It should be noted that the primary process is conducted in the spectral domain by analyzing the phase of the cross-spectrum. This enables the precise selection of the desired frequency band based on the coherence between the two windowed cross-correlations. Each measured delay-time corresponds to the central point of the window and is determined from the cross-correlation lag-time. Subsequently, the second step involves analyzing the trend of the delay-time estimates over the entire length of the signals, resulting in the evaluation of the $\delta t/t$. The linear regression of the delay-time estimates provides a rough indication of the relative homogeneous velocity perturbation between the current cross-correlation and the reference cross-correlation (James et al., 2017).

In the MWCS analysis, several critical parameters need to be considered, including the selection of N_{ref} and N_{cur} , the length and overlap of each window, and the total number of windows used in the analysis. These parameters are crucial to the initial process and depend on the characteristics of the cross-correlation functions, such as their length and frequency content, as well as the speed at which the signal decays below the noise level. The primary step in the MWCS analysis involves computing the delay-times (δt) between two cross-correlation functions within a series of intersecting lag-time windows. Each cross-correlation function is

partitioned into N_w windows, with each window corresponding to a delay-time measurement. The selection of window length, overlap, and N_w will typically be influenced by the frequency characteristics and signal-to-noise ratios (SNRs) of the cross-correlation functions in question. The cross-spectrum $X(v)$, between the two segmented time-series is then obtained as follows:

$$X(v) = F_{ref}(v) \cdot F_{cur}^*(v) \quad (1)$$

where $F_{ref}(v)$ and $F_{cur}(v)$ represent the Fourier-transformed versions of the time-series, which have been windowed. Here, v represents frequency in Hz, and the asterisk indicates complex conjugation. It is more appropriate to describe the complex cross-spectrum in terms of its amplitude $|X(v)|$ and phase $\phi(v)$

$$X(v) = |X(v)| e^{i\phi(v)} \quad (2)$$

The time-shift between the two cross-correlations can be determined from the (unwrapped) phase spectrum, $\phi(v)$, of the cross-spectrum, which exhibits a linear relationship with frequency.

$$\phi_j = m \cdot v_j \quad m = 2\pi\delta t \quad (3)$$

To calculate the time delay in each window, first, determine the frequency range of interest. Then, calculate the phase displacement in each frequency for each window. Next, apply linear regression to the phase displacements along the frequencies of interest. According to Equation (3), the slope of this linear regression is the time delay. Repeat this process for all time series windows. Since the time series is a function of time, the time delay obtained for each window can be plotted as a function of time. To determine the velocity perturbation dv/v , apply linear regression to the time delays for all windows. This time, the slope of the regression represents the velocity perturbation according to Equation (4) (Clarke et al., 2011).

$$\frac{\delta t}{t} = - \frac{\delta v}{v} \quad (4)$$

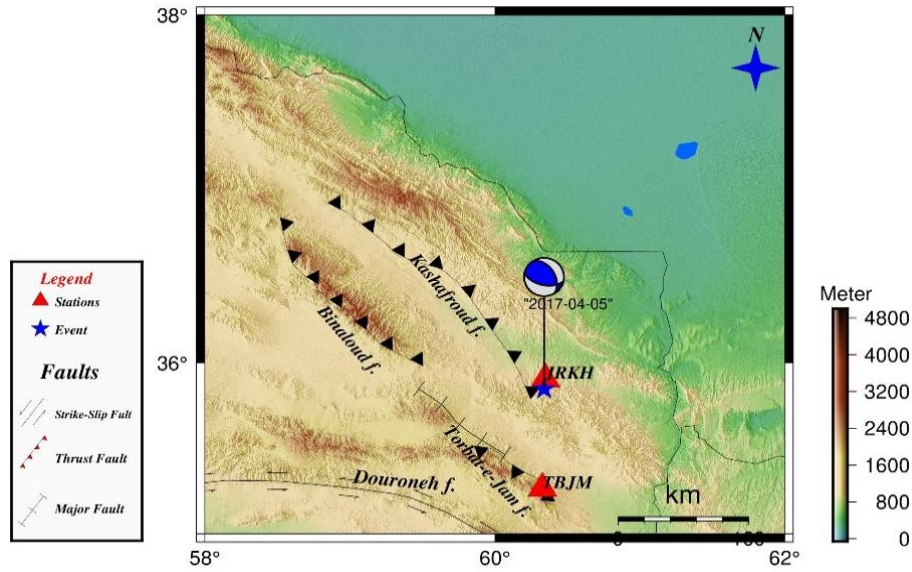


Figure 1. Geographical location of Mashhad seismic network stations.

3-6. Data Processing

MSNoise software was employed to calculate velocity changes using the vertical component data as software input (Lecocq et al., 2014). In calculating cross-correlation, 24-hour continuous data periods were first divided into 30-minute periods, and cross-correlation was then calculated for these 30-minute waveforms. The resulting correlated functions were linearly stacked over a 24-hour period, and a waveform was obtained for each day. The first 90 days of the entire study period were stacked and considered as the reference function, while current functions were derived from 5, 10, 15, and 30-day stacks (Figure 2). In the Moving Window Cross-Spectral method, it is often desirable to exclude ballistic waves from the analysis because they do not provide information about the scattering properties of the Earth's interior, which is the primary focus of this method. Instead, the analysis aims to capture the scattered waves that arrive later, which carry information about the Earth's structure and velocity changes. By visually inspecting the Green's function, we concluded that elastic waves enter for up to 25 seconds. Therefore, for greater certainty, we considered starting the lag from 30 seconds.

To calculate the time delay, both the causal

and non-causal parts of the correlation functions were used within the time intervals of 30 to 120 seconds and -30 to -120 seconds. The window lengths were set equal to the duration of the longest period in the correlation function, with an 80% overlap applied between the windows.

The maximum error in the regression line for calculating the time delay is considered to be 0.1 seconds. By setting this threshold, you ensure that only data points with relatively high precision (i.e., low error) are included in the analysis. This helps maintain the accuracy and reliability of the results by excluding data points with high uncertainty.

We considered a minimum value of 0.01 for the maximum stretching coefficient. The stretching parameter is determined by finding the factor that maximizes the correlation coefficient between the stretched current waveform and the reference waveform.

Equation (5) was implemented to calculate the cross coherence $C(v)$ between the energy densities of two functions, and any values lower than the minimum threshold of 0.65 were excluded from the calculations.

$$C(c) = \frac{\overline{|x(v)|}}{\sqrt{\overline{|F_{ref}(v)|^2} \cdot \overline{|F_{cur}(v)|^2}}} \quad (5)$$

Here, the overlines indicate smoothing.

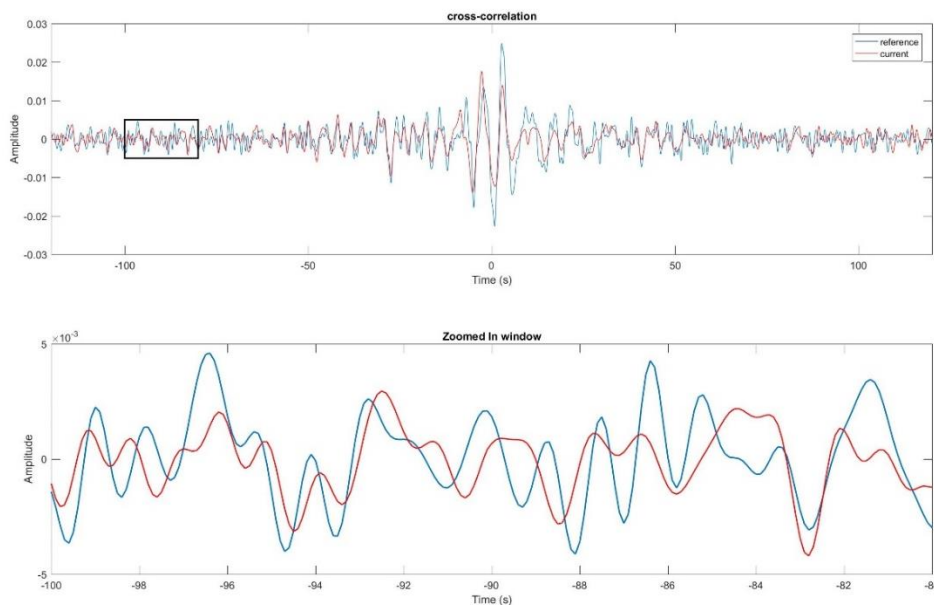


Figure 2. Current function applied to the reference function for calculating phase differences within specified time windows. The phase displacement is calculated for all frequencies. Then, a linear regression is applied to all measured phase displacements. The slope of this regression equals the time delay for the desired window. This process is repeated by moving the window across the entire signal and calculating the time delay at each position.

IR.JRKH-IR.TBJM f3 m30 2017-04-05

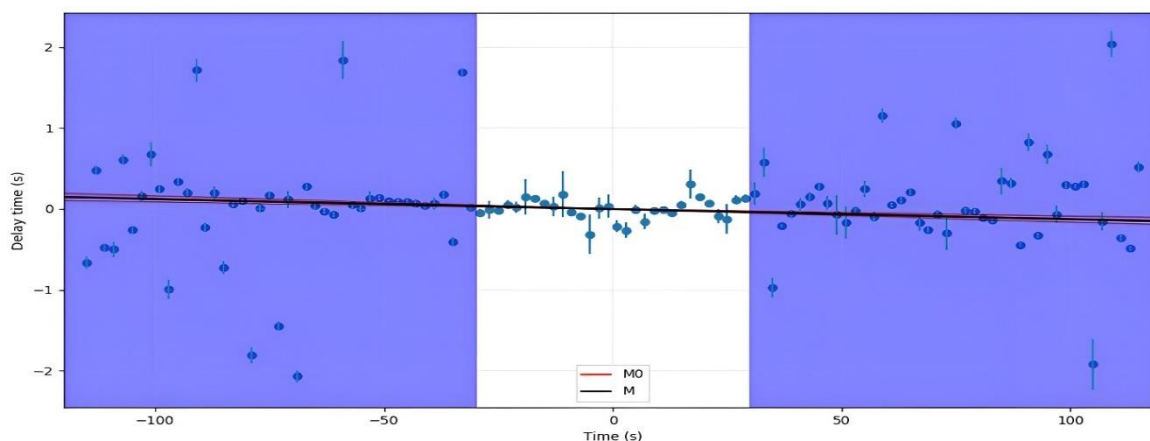


Figure 3. This plots dt (delay time) against t (time lag). It shows the results from the MWCS step, plus the calculated regression lines $M0$ and M . The errors in the regression lines are also plotted as fainter lines. The time lags used to calculate the regression are shown in blue. $M0$: Weighted Least Squares (WLS) with Origin Constraint. M : WLS with Offset.

4. Result and Discussion

Monitoring processes in damage zones represents significant challenges due to their unique characteristics. These zones tend to have spatially localized structures with low elastic moduli and high rock susceptibility. As a result, traditional monitoring techniques may fail to provide accurate assessments of the processes occurring within these zones (Hillers and Campillo, 2016). The evolution of velocity related to earthquakes can happen at extremely different scales and amplitudes, which may not be detectable through seismic interferometry. As a result, linking these shifts

to laboratory experiments can be particularly difficult.

Seismic ambient noise propagates as seismic waves through different layers of the Earth, resulting in complex wave patterns. As these waves encounter various layers, they can be reflected, refracted, and scattered based on the physical properties of each layer. By analyzing and measuring these patterns, a better understanding of the Earth's structure can be obtained.

The depth of origin of ambient seismic noise can vary depending on the frequency range being analyzed and the location of the sensors.

In general, low-frequency vibrations (below 1 Hz) can penetrate deeper into the Earth's crust, while higher-frequency vibrations have a more shallow depth of origin. However, it is important to note that the actual depth of the source of seismic noise can vary based on several factors such as the geology of the area and the propagation properties of the medium through which the seismic waves travel.

In this study, we considered the hypocenter depth to be 10 km, as well as varying depths, to monitor velocity changes leading up to the earthquake. As mentioned earlier, the MWCS method consists of two basic steps. In the first step, we calculate the phase displacement for various frequencies and apply linear regression to all the phase displacements. The slope of this regression provides us with the time delay within that specific window. The frequency range influences the slope of the line. We began with a narrow range and progressively expanded to wider ranges.

To investigate the narrow frequency range at varying depths, it is essential to apply specific bandpass filters. In this study, we utilized filters with frequency ranges of 0.2 to 0.4 Hz,

0.4 to 0.6 Hz, 0.6 to 0.8 Hz, and 0.8 to 1.0 Hz. The length of the window used to perform calculations was determined based on the specific filter applied. Specifically, the length of the window for each frequency band was set to equal the maximum period associated with that particular bandpass filter. Throughout the entire period, velocity fluctuations can be observed in each of the examined narrow ranges (Figure 4). As previously mentioned, these fluctuations can have different underlying causes. Despite implementing certain strategies, such as increasing the overlap of windows, using different parts of the signal, and setting a minimum cross coherence, no significant deviations related to earthquakes were observed in any of the investigated ranges.

The primary reason for these variations is the regression slope applied to the phase displacement. In small ranges, the number of data points used for regression is limited. Consequently, the presence of several outlier phase displacements can cause significant changes in the regression slope, ultimately leading to large fluctuations in the final results.

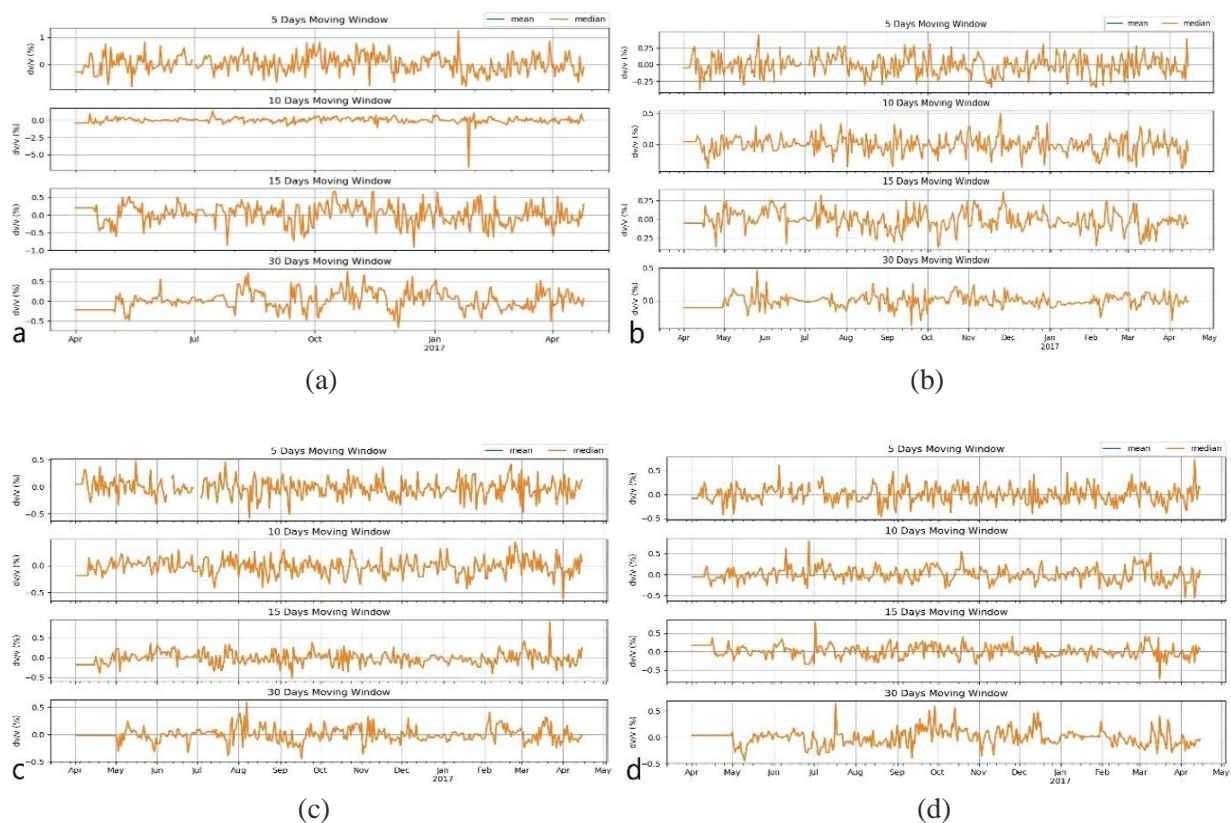


Figure 4. Velocity change for frequency a) 0.8 to 1.0 Hz, b) 0.6 to 0.8 Hz, c) 0.4 to 0.6 Hz, d) 0.2 to 0.4 Hz.

Identifying the contributing factors towards the alterations of seismic wave velocity is a formidable undertaking, as these factors often interact in complex manner. These amendments may also exert a profound influence on other factors, either fortifying or diminishing their impact. In volcanic regions, for instance, an increase in velocity attributed to elevated pressure may be counteracted by a decrease caused by the presence of hot magma (Liu et al., 2022).

As noise waves repeatedly traverse through various layers, they exhibit a remarkable degree of sensitivity toward alterations and magnify even small variations. Furthermore, this sensitivity increases with distance, making noise waves particularly responsive to changes occurring in the fault zone. Since the fault zone covers a wide range of depths and levels, rendering the entire zone vulnerable to changes in stress and strain levels, it was deemed necessary to conduct an investigation on wider frequency range so as to gain a more comprehensive understanding of these changes. On the other hand, in a wide frequency range, the effect of outlier data on regression is reduced.

During our investigation process, we delved deeper into the wider range by introducing 0.2 to 1 Hz filters. The narrow frequency range showed notable fluctuations in velocity change, whereas we found that the wider frequency range exhibited smoother velocity change fluctuations. We calculated the difference between the initial and final values of the velocity changes from the beginning to the end of the incremental process. This calculation was performed for all four stacking groups. We then considered the average value of these differences as the velocity change preceding the earthquake. By analyzing the pattern of velocity changes, we observed a rising trend of 0.3% over the two months leading up to the earthquake. This percentage increase is approximately 0.1% higher than the maximum value that was observed during the entire period preceding the earthquake (Figure 5). This observed increase in velocity is comparable to the findings of Wegler et al. (2006), who reported an increase in velocity in the fault zone associated with the Mw = 6.6 Mid-Niigata earthquake for 1.5 months before the event.

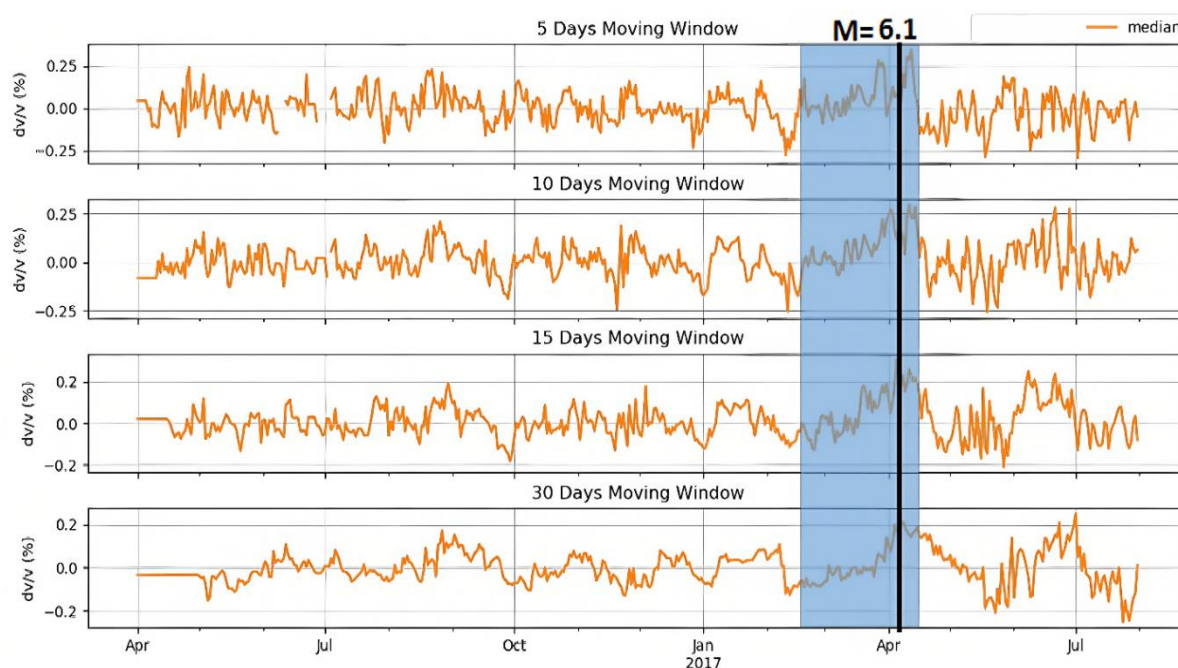


Figure 5. Velocity change for frequency 0.2 to 1.0 Hz. The black line indicates the day of the earthquake. Discernible increasing trends in fault zone velocity changes are observable. However, the most significant trend is the most recent recorded increase, which reached its highest value and coincided with a seismic event. We propose that this heightened velocity change is influenced by the intensifying effects of the stress field, which interacts with pre-existing factors such as seasonal variations.

Throughout the entire studied period, there are observable increasing trends in velocity changes. However, the most recent recorded trend is of particular interest, as it experienced its highest value and resulted in an earthquake. We believe this phenomenon is due to the intensifying effects of the stress field on other previously existing factors. By utilizing the method presented in this study, the impacts of individual factors can be observed and in the event that a new factor arises to impact previous factors, this effect will manifest as deviant behavior from established patterns.

The accuracy of using this method can depend on the number of days of stacking in the preparation of Green's functions. As the number of stacking days increases, the ability to access instantaneous changes can become limited. This study investigated the effects of using stacks with durations ranging from 5 to 30 days on the accuracy of velocity change calculations. The results revealed that this range of stacking days posed challenges in achieving instantaneous changes, leading to reduced accuracy. Nevertheless, the approach proved to be useful for identifying trends. An increasing number of stack days made it easier to discern trends, thereby enhancing the visibility of the changes.

After the earthquake, we anticipated a sudden alteration in the rate of velocity change. However, due to the implementation of green function stacking, we were unable to acquire instantaneous changes and instead found a downward trend in the rate of velocity change over time. Prior research has shown that reductions in velocity caused by earthquakes are linked to dynamic changes in stress and strain, rather than static changes (e.g., Rubinstein and Beroza, 2004; Hobiger et al., 2016; Brenguier et al., 2014). These changes can be attributed to the formation and enlargement of cracks due to intense ground shaking (Wu et al., 2009). Nevertheless, the observed reduction in velocity changes following the earthquake, which aligns with the findings of Ikeda and Tsuji, suggests a

similar pattern. In their study, they investigated the $M_w = 5.9$ earthquake in the Nankai subduction zone and documented a clear decrease in seismic velocity at the time of the earthquake.

A visual examination of Green's function revealed that, after the earthquake, larger amplitudes were observed throughout the entire length of the signal. In contrast, before the earthquake, these amplitudes were mostly confined to the initial part (Figure 6). Earthquakes can create or modify scatterers within the Earth's crust, which can increase the complexity of the seismic wavefield. This can result in more reverberated signals (coda) and a greater number of peaks in the Green's function, especially at the ends, indicating a more complex wave propagation environment.

We also evaluated the correlation coefficient between the reference function and the current functions (Figure 7). The findings indicated a high correlation coefficient between the reference function and the obtained current functions, with an approximate average value of 0.8 before the earthquake. However, as soon as the earthquake, the correlation coefficient value began to decline and eventually dropped below 0.5. After the earthquake, the movement of the scatterers caused changes in ambient noise, as noted by Hadziioannou et al. (2009). Additionally, successive aftershocks altered the shape of the cracks, leading to the acquisition of different green functions.

Future research directions should focus on refining the MWCS technique to enhance its sensitivity to transient changes and exploring the integration of additional data sources, such as geological and geophysical measurements, to provide a more comprehensive understanding of the factors influencing seismic velocity changes. By contextualizing our findings within the existing literature and emphasizing their contributions to the field, we aim to advance the understanding of earthquake hazards and improve monitoring strategies in fault zones.

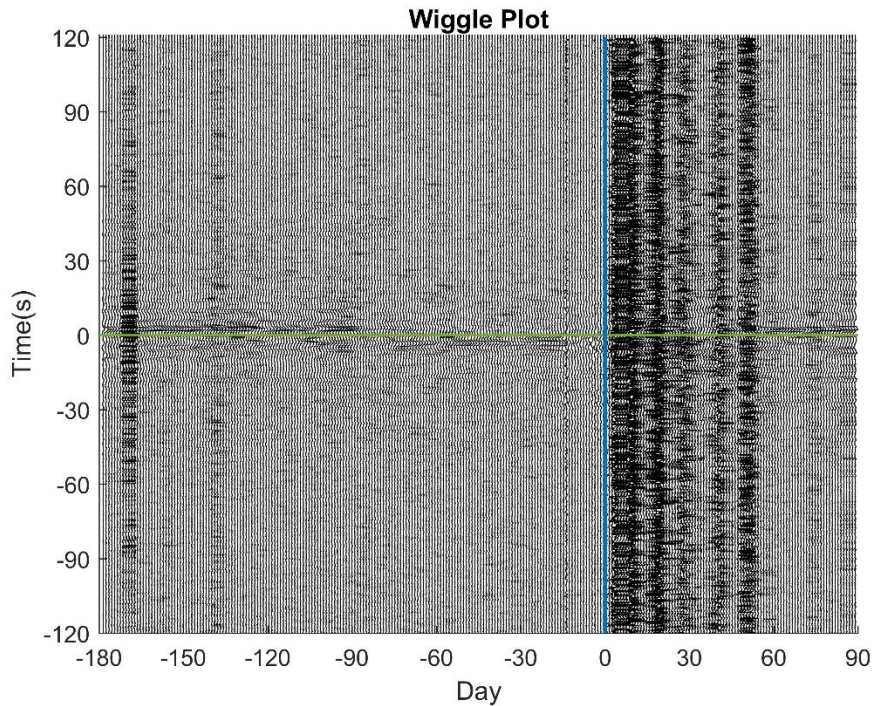


Figure 6. Continuous plot of the Green's function resulting from 5-day stacking. The green line corresponds to the zero shift in the Green's function, and the blue line indicates the day of the earthquake.

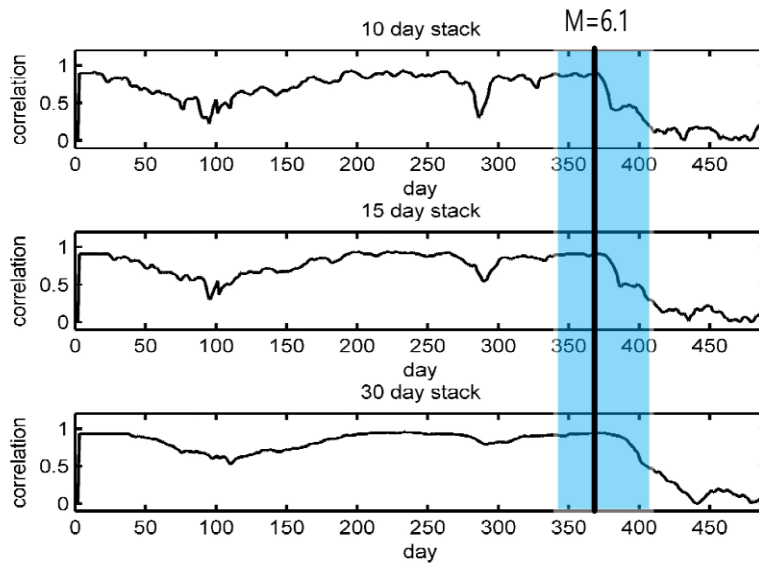


Figure 7. Correlation coefficients between reference and current functions for current functions obtained from a 10 to 30-day stack.

5. Conclusion

This study has provided valuable insights into the complexities of monitoring velocity changes in seismological research. Our findings reveal that the width of the frequency range significantly influences the results, with narrower ranges leading to severe fluctuations that hinder interpretation. In contrast, broader frequency ranges yield smoother data, allowing for clearer trends in velocity changes.

Additionally, the analysis of Green's functions demonstrates that the number of stacking days plays a crucial role in the resolution of our findings. While increasing the number of stacking days enhances the clarity of velocity trends, it limits the ability to analyze short-term intervals, which is essential for identifying specific seismic events.

Importantly, our results indicate a consistent pattern of increasing velocity in the months leading up to an earthquake, peaking just days

before the event. This observation suggests a potential link between pre-fracture states and static factors, highlighting the need for further investigation into these dynamics. Post-earthquake data revealed a decelerating trend rather than the anticipated abrupt changes, possibly due to the stacking effect of pre-earthquake Green's functions.

Overall, this research underscores the challenges of monitoring velocity changes in the context of ambient noise and local geological structures. It emphasizes the need for careful consideration of methodological parameters and suggests that further studies could refine our understanding of seismic precursors and their implications for earthquake prediction.

References

- Aflaki, M., Mousavi, Z., Ghods, A., Shabaniyan, E., Vajedian, S., & Akbarzadeh, M. (2019). The 2017 Mw 6 Sefid Sang earthquake and its implication for the geodynamics of NE Iran. *Geophysical Journal International*, 218(2), 1227–1245. <https://doi.org/10.1093/gji/ggz172>
- Brenguier, F., Campillo, M., Takeda, T., Aoki, Y., Shapiro, N. M., Briand, X., Emoto, K., & Miyake, H. (2014). Mapping pressurized volcanic fluids from induced crustal seismic velocity drops. *Science*, 345, 80–82. <https://doi.org/10.1126/science.1254073>
- Brenguier, F., Shapiro, N. M., Campillo, M., Nercissian, A., & Ferrazzini, V. (2008). Towards forecasting volcanic eruptions using seismic noise. *Nature Geosci*, 1, 126–130. <https://doi.org/10.1038/ngeo104>
- Clarke, D., Zaccarelli, L., Shapiro, N. M., & Brenguier, F. (2011). Assessment of resolution and accuracy of the Moving Window Cross Spectral technique for monitoring crustal temporal variations using ambient seismic noise. *Geophysical Journal International*, 186(2), 867–882. <https://doi.org/10.1111/j.1365-246X.2011.05074.x>
- Crampin, S., & Zatsepin, S. V. (1997). Modelling the compliance of crustal rock—II. Response to temporal changes before earthquakes. *Geophysical Journal International*, 129(3), 495–506.
- Ghayournajarkar, N., & Fukushima, Y. (2020). Determination of the dipping direction of a blind reverse fault from InSAR: case study on the 2017 Sefid Sang earthquake, northeastern Iran. *Earth, Planets and Space*, 72(1), 1–18. <https://doi.org/10.1186/s40623-020-01190-6>
- Grêt, A., Snieder, R., & Scales, J. (2006). Time-lapse monitoring of rock properties with coda wave interferometry. *Journal of Geophysical Research: Solid Earth*, 111(B3). <https://doi.org/10.1029/2004JB003354>
- Hadziioannou, C., Larose, E., Coutant, O., Roux, P., & Campillo, M. (2009). Stability of monitoring weak changes in multiply scattering media with ambient noise correlation: Laboratory experiments. *The Journal of the Acoustical Society of America*, 125(6), 3688–3695.
- Hillers, G., & Campillo, M. (2016). Fault zone reverberations from cross-correlations of earthquake waveforms and seismic noise. *Geophys. J. Int.*, 204, 1503–1517. [doi:10.1093/gji/ggv515](https://doi.org/10.1093/gji/ggv515)
- Hobiger, M., Wegler, U., Shiomi, K., & Nakahara, H. (2016). Coseismic and post-seismic velocity changes detected by passive image interferometry: comparison of one great and five strong earthquakes in Japan. *Geophys J Int*, 205, 1053–1073. <https://doi.org/10.1093/gji/ggw066>
- James, S. R., Knox, H. A., Abbott, R. E., & Sreaton, E. J. (2017). Improved moving window cross-spectral analysis for resolving large temporal seismic velocity changes in permafrost. *Geophysical Research Letters*, 44(9), 4018–4026. <https://doi.org/10.1002/2016GL072468>
- Lecocq, T., Caudron, C., & Brenguier, F. (2014). MSNoise, a Python Package for Monitoring Seismic Velocity Changes Using Ambient Seismic Noise. *Seismological Research Letters*, 85(3), 715–726. [doi: 10.1785/0220130073](https://doi.org/10.1785/0220130073)
- Liu, Z., Liang, C., Huang, H., Wang, C., & Cao, F. (2022). Seismic velocity variations at different depths reveal the dynamic evolution associated with the 2018 Kilauea eruption. *Geophysical Research Letters*, 49(3), e2021GL093691.
- Nameni, M. R., Jafari, S., & Rahimi, H. (2024). Filling the gap of seismic ambient noise taken from the earth by modification of the frequency content of the existing time series. *Arab J Geosci*, 17, 87.

- <https://doi.org/10.1007/s12517-024-11863-1>
- Nedaei, M., & Alizadeh, H. (2020). New insights into the 2017 Sefidsang earthquake by Coulomb stress change pattern and aftershock distributions: implication for active tectonics of NE Iran. *Geopersia*, 10(2), 351-365. <https://doi.org/10.22059/GEOPE.2020.299725.648538>
- Petrova, N. V., Bezmenova, L. V., & Kurova, A. D. (2022). Earthquake of April 5, 2017, MW = 6.0, in Northeast Iran: Focal parameters, aftershock series, and macroseismic manifestations. *Geophysical Survey, Russian Academy of Sciences*. <https://doi.org/10.3103/S0747923922070088>
- Poupinet, G., Ellsworth, W. L., & Frechet, J. (1984). Monitoring velocity variations in the crust using earthquake doublets: an application to the Calaveras faults, California. *Journal of Geophysical Research*, 89(B7), 5719-5731. <https://doi.org/10.1029/JB089iB07p05719>
- Rubinstein, J. L., & Beroza, G. C. (2004). Evidence for widespread nonlinear strong ground motion in the MW 6.9 Loma Prieta earthquake. *Bull Seismol Soc Am*, 94, 1595–1608. <https://doi.org/10.1785/012004009>
- Sens-Schönfelder, C., & Wegler, U. (2006). Passive image interferometry and seasonal variations of seismic velocities at Merapi Volcano, Indonesia. *Geophysical Research Letters*, 33(21). <https://doi.org/10.1029/2006GL027797>
- Sens-Schönfelder, C., & Wegler, U. (2007). Fault zone monitoring with passive image interferometry. *Geophysical Journal International*, 168(3), 1029–1033. <https://doi.org/10.1111/j.1365-246X.2006.03284.x>
- Tape, C., Liu, Q., Maggi, A., & Tromp, J. (2010). Seismic tomography of the southern California crust based on spectral-element and adjoint methods. *Geophysical Journal International*, 180(1), 433-462. <https://doi.org/10.1111/j.1365-246X.2009.04429.x>
- Wu, C., Peng, Z., & Ben-Zion, Y. (2009). Non-linearity and temporal changes of fault zone site response associated with strong ground motion. *Geophys J Int*, 176, 265–278. <https://doi.org/10.1111/j.1365-246X.2008.04005.x>